Journal of Solid State Chemistry 308 (2022) 122906

Contents lists available at ScienceDirect

Journal of Solid State Chemistry

journal homepage: www.elsevier.com/locate/jssc

Advances in the understanding of mesoporous transition aluminas: Unveiling the correlation between morphology and thermostability

Marcos Schöneborn [a,*], Jonas Werner [b], Thomas Harmening [a], Thomas E. Weirich [b]

[a] SASOL Germany GmbH, Advanced Materials Division, Anckelmannsplatz 1, 20537, Hamburg, Germany
[b] RWTH Aachen University, GFE Central Facility for Electron Microscopy, 52074, Aachen, Germany

ARTICLE INFO

Keywords:
Catalyst support
Transition alumina
Thermostability
Phase transformation
ACOM-TEM

ABSTRACT

The thermostabilities of mesoporous γ-Al_2O_3 samples with similar initial surface areas and average pore radii, but significantly different pore volumes, were studied in detail. The results show that γ-Al_2O_3 with highest initial pore volume converts to α-Al_2O_3 at a significantly higher temperature, along with larger residual surface area and pore volumes after aging. These observations are directly related to the morphologies of the individual particles and the resulting aggregate structures, which were studied by automated crystallite orientation mapping (ACOM-TEM). Large particles with well-developed plate-like morphologies preferentially form dense stacks by assembly via the {110} main basal planes (pseudo-cubic lattice). This arrangement favors sintering and the formation of α-Al_2O_3 at comparatively low temperatures. Aluminas with higher proportions of the lateral {100} and {111} facets tend to form aggregate structures with higher porosities and lower interparticle contact areas, thus explaining their superior thermostabilities. These findings highlight the importance of the aggregate structure for the purposeful development of alumina-supported catalysts.

1. Introduction

Mesoporous transition aluminas are widely-used support materials for heterogeneous catalysts in a variety of industrial applications, like Fischer-Tropsch synthesis, naphta reforming, and automotive emission control, due to their high surface areas, adjustable porosities and beneficial metal-support interactions [1–4].

Despite the increasing relevance of electromobility, gasoline powered vehicles will still play an important role in the next couple of years. The upcoming tighter global emissions legislation, like Euro 7, will not only include stricter thresholds for pollutants but also much more demanding requirements as to the long-time durability of the catalytic converters. In addition, a lot of attention is nowadays drawn to new powertrain concepts aiming at reduced CO_2 emissions to mitigate the climate change. Some of these approaches still rely on internal combustion engines and are considered to supplement the efforts based on electrification. These include the use of fuels based on renewable feedstock (biofuels), and the production of fuels using energy from renewable sources, such as wind and solar energy [5]. In this regard, the idea behind the Power-to-X technology is to use these energy sources for the production of green hydrogen, which can then be used to convert CO_2 into synthetic fuels (eFuels) and other chemicals [6]. Alternatively, the generated hydrogen could be stored and used in hydrogen combustion engines. Although the occurrence of pollutants originating from the combustion of organic compounds is ruled out in this concept, NO_x emissions are perpetual challenges and will require proper catalytic after-treatment, for instance by H_2-assisted selective catalytic reduction (H_2–NH_3-SCR) using Ag/Al_2O_3 catalysts [7–10]. It is more than likely that the introduction of said alternative fuels and powertrain concepts in the future will also lead to new requirements for the catalytic converters. This calls for a better understanding of the different mechanisms leading to catalyst deactivation, and for the design of new and improved catalysts.

Sintering, along with the formation of α-Al_2O_3, is one of the most important deactivation mechanisms of alumina-supported catalysts used in high-temperature applications, as it is associated with drastic decrease of surface area and pore volume, so that noble metal sintering and encapsulation are inevitable to occur [11]. Detailed understanding of the parameters controlling these phenomena is thus of pivotal importance for the design of transition aluminas with improved thermal durability.

A common approach for the preparation of metastable γ-Al_2O_3 with high specific surface area is the topotactic dehydroxylation of boehmite (γ-AlOOH) at temperatures of at least 300 °C. The phase transition γ-AlOOH → γ-Al_2O_3 progresses in a pseudomorphic manner, so that the morphology and pore structure defined at the stage of the boehmite are

* Corresponding author.
E-mail address: marcos.schoeneborn@de.sasol.com (M. Schöneborn).

https://doi.org/10.1016/j.jssc.2022.122906
Received 8 November 2021; Received in revised form 10 January 2022; Accepted 11 January 2022
Available online 19 January 2022

preserved in the resulting γ-Al_2O_3 [12,13].

Calcination at higher temperatures leads to the formation of other transition aluminas, and finally the thermodynamic stable α-Al_2O_3: γ-AlOOH → γ-Al_2O_3 → δ-Al_2O_3 → θ-Al_2O_3 → α-Al_2O_3 [14,15].

Common structural features of the transition aluminas γ, δ and θ are the oxide sublattices equivalent to that of the closest cubic packaging (ccp), and the partial occupancy of the available tetrahedral (T_d) and octahedral (O_h) sites by aluminium(III). The irreversible phase transitions γ-Al_2O_3 → δ-Al_2O_3 → θ-Al_2O_3 lead to crystal structures with reduced symmetries allowing for an increasing positional order of Al(III) like vacancies among the available T_d and O_h positions, such as to an increasing population of T_d sites [13,15,16].

The crystal structure of γ-Al_2O_3 is often described as a "defect spinel" structure with cubic symmetry which corresponds to that of the aristotype spinel structure of $MgAl_2O_4$ (*Fd* $\bar{3}$ *m*, No. 227) [17]. The structure of γ-Al_2O_3 shows a high degree of positional disorder of aluminium(III) and vacancies among the T_d and O_h sites within the array of oxide ions. The relationship to the spinel structure and the abundance of cationic vacancies can be illustrated by the notation "$\square^{Td/Oh}_{1/3}Al^{Td/Oh}_{8/3}O_4$". In investigations by Zhou et al., it was found that aluminium(III) preferably populates O_h sites in γ-Al_2O_3, which is the most important difference to the crystal structure of Bayerite-derived η-Al_2O_3, exhibiting significantly higher site occupancy factors for the T_d sites [13]. More detailed investigations employing several sophisticated analytical tools, like solid-state NMR spectroscopy and synchrotron powder X-ray diffraction, favor the "Tetragonal-8c" model with space-group *I*4_1*/amd* (No. 141). This structure model also involves a partial occupancy of non-spinel sites with aluminium(III) in octahedral coordination [18,19].

The determination of the real structural nature of δ-Al_2O_3 has been subject of several studies. Jayaram et al. suggested the symmetry to be orthorhombic (*P*$2_12_12_1$, No. 19), which they concluded from systematic absences in electron diffraction experiments. However, a suitable orthorhombic structure model was not established [20]. Repelin et al. reported a tetragonal structure model (P $\bar{4}$ m2, No. 115), which they determined from X-ray and electron diffraction data, and which can be regarded as a superstructure of γ-Al_2O_3 [21]. Detailed studies by Kovarik et al. uncovered the existence of at least four different phases, which coexist as complex intergrowth structures, and which exhibit different symmetries: δ$_1$-Al_2O_3: *P*$2_12_12_1$, No. 19; δ$_2$-Al_2O_3: *P*2_1, No. 4; δ$_3$-Al_2O_3: *A2/n*, No. 15; δ$_4$-Al_2O_3: *P* $\bar{1}$, No. 2 [22–24].

The crystal structure of θ-Al_2O_3 is isotypic to that of β-Ga_2O_3 (*C2/m*, No. 12) and features an ordered and equal distribution of Al(III) among the available T_d and O_h sites (Fig. 1a) [13,25]. In addition to this well-known structure, Kovarik et al. reported about the existence of a disordered composite structure occurring at the high temperature region of the θ-Al_2O_3 stability range after long annealing times [23].

Calcination at higher temperatures (>1100 °C) leads to the formation of the thermodynamically stable polymorph α-Al_2O_3, resulting from a reconstructive phase transition (θ → α). α-Al_2O_3 adopts the trigonal corundum crystal structure with rhombohedral Bravais lattice (*R* $\bar{3}$ *c*, No. 167), in which the arrangement of oxide ions corresponds to the hexagonal closest packaging (hcp). In this structure, aluminium(III) exclusively occupies O_h sites leading to [AlO_6] octahedra, which share edges in the (110) plane and faces along the [001] axis (Fig. 1b).

The formation of α-Al_2O_3 progresses via a nucleation-growth mechanism. It is initiated by the dehydroxylation of the alumina surfaces in the neck regions of adjacent crystallites in which OH-groups are in close contact. The as-created anionic vacancies and intrinsically abundant surface-near cationic vacancies annihilate each other, whereby the structure is rearranged and α-Al_2O_3 nuclei are formed [26,27]. The mechanism can be expressed in Kröger-Vink notation as follows:

(1) alumina composition: $(Al_{Al})_2\ V''_M O_{O3-\upsilon/2}\ (OH'_O)_\upsilon\ V''_{O1-\upsilon/2}\ (\upsilon = 0–2)$

(2) dehydroxylation: $2(OH'_O) \rightarrow H_2O + O_O + V''_O$

(3) annihilation: $V''_O + V''_M \rightarrow 0$

Al_{Al}: aluminium(III) on T_d or O_h positions, V''_M: cationic vacancies on T_d or O_h positions, OH'_O: OH-groups on oxide positions, V''_O: anionic vacancies on oxide positions.

Formula (1) captures the compositions of boehmite ($\nu = 2$), α-Al_2O_3 ($\nu = 0$) and the transition aluminas with varying concentrations of surface hydroxyls [27].

The growth of neck regions at the reactive surface proceeds via continued condensation of hydroxyl groups associated with progressive sintering, which explains the drastic loss of surface area associated with

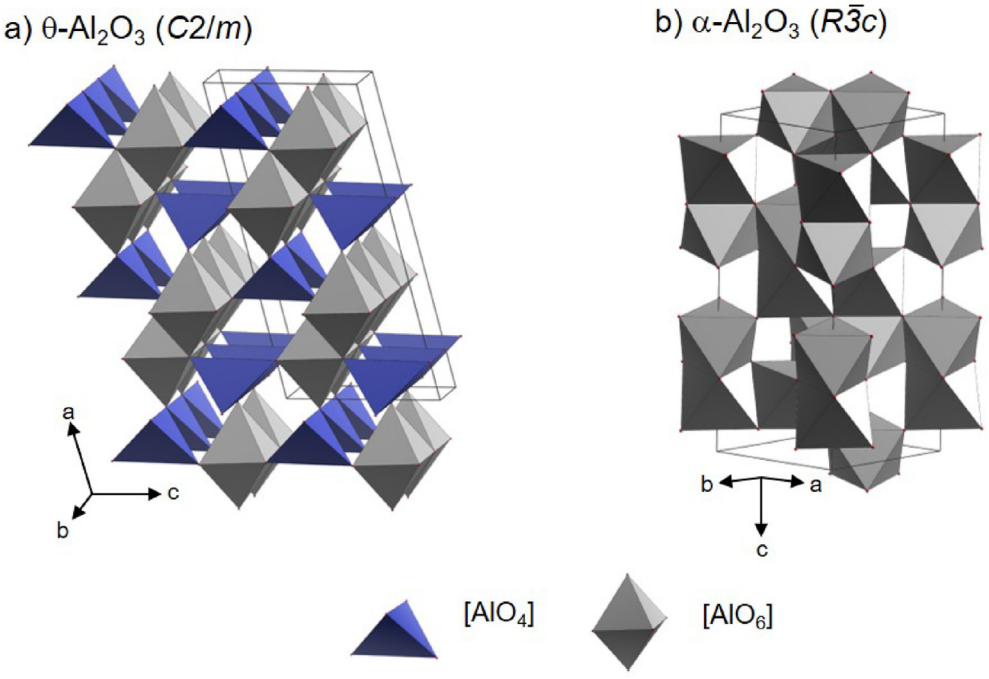

Fig. 1. Crystal structures of a) θ-Al_2O_3 and b) α-Al_2O_3, highlighting the significant structural changes resulting from the reconstructive phase transition θ → α.

the formation of α-Al_2O_3.

There is broad consensus that the rate of α-Al_2O_3 formation depends on the crystallite size of the starting boehmite and the surface area of the initial transition alumina. It has been found that higher initial surface areas favor sintering, and thus the transformation to α-Al_2O_3 at lower temperatures [27–29]. In addition, Lee et al. reported about superior thermostabilities of rod- and platelet-shaped aluminas [30]. However, the samples studied in this work also varied markedly in terms of initial surface areas, so that the different rates of sintering can most likely not solely be attributed to the morphological peculiarities.

In order to provide a deeper understanding of the impact of the aggregate structure on the thermostabilities of transition aluminas, we studied three different commercially available γ-Al_2O_3 samples exhibiting similar surface areas (132–158 m^2/g) and average pore radii (11.3–14.6 nm), but which differ significantly in their pore volumes (0.64–1.18 cm^3/g) stemming from different primary particle morphologies and assemblies.

The thermostability of the samples was studied via N_2-adsorption/desorption, differential scanning calorimetry (DSC) and powder X-ray diffraction (XRD).

Particle size distributions, morphologies and aggregate structures of the γ-Al_2O_3 samples were systematically investigated by transmission electron microscopy (TEM) using conventional bright field imaging and automated crystallite orientation mapping (ACOM) by means of scanning electron nanobeam diffraction (SEND).

2. Experimental section

2.1. Materials

The transitional aluminas PURALOX 100/130 ("P100"), PURALOX TM100/150 ("TM100") and PURALOX TH100/150 ("TH100") studied in this work are commercially available from SASOL. The materials are produced via an alkoxide-based process which includes the formation and processing of boehmites with subsequent calcination at elevated temperature to obtain the final transition aluminas. All samples are of high purity (>99.9%), so that any effects arising from impurities can be excluded in the present study. The samples were aged in air at 1000 °C for 3 h, at 1100 °C for 3 h and 10 h, and at 1200 °C for 3 h and 10 h for the investigation of their thermostabilities.

2.2. Characterization of materials

Surface areas (Brunauer-Emmett-Teller method, BET), pore volumes and pore radius distributions (Barrett–Joyner–Halenda method, BJH) of the samples were determined by N_2-adsorption and desorption at −196 °C, using a Quantachrome Quadrasorb SI instrument. Prior to analysis, samples were outgassed under vacuum for 30 min at 300 °C. X-ray powder diffraction was conducted on a Phillips X'Pert diffractometer, using Cu-K_α radiation ($\lambda = 1.540598$ Å). Powder diffractograms were recorded between 5° and 90° (2θ), with a step-width of 0.02°. The PANalytical X'Pert Highscore Plus software was used for phase identification and simulation of X-ray powder patterns. Differential scanning calorimetry (DSC) experiments were conducted on a Netzsch STA 449 C Jupiter thermal analyzer. Approximately 20 mg per fresh sample were heated under air from 30 to 1500 °C at a heating rate of 10 K/min.

(Scanning) Transmission electron microscopy ((S)TEM) investigations were performed with a 200 kV Libra200FE (Carl Zeiss Microscopy GmbH) equipped with a charge-coupled device (CCD) camera (Gatan Inc.), a 200 kV Tecnai F20 (FEI Company) equipped with an ASTAR system (NanoMEGAS SPRL), as well as a 200 kV JEM-F200 (JEOL (Germany) GmbH) equipped with an annular dark field (ADF) detector, a secondary electron (SE) detector and an ASTAR system. Digital Micrograph (Version 2.11.1404.0, Gatan Inc.) was used for image processing [31] and analysis of TEM bright field (BF)-, STEM-ADF- and SE images. Scanning electron nanobeam diffraction (SEND) and subsequent automated crystallite orientation mapping (ACOM, ASTAR system) [32] was used for orientation and crystallite size distribution analysis. Acquired data was processed with the ASTAR-included software package using diffraction pattern templates based on cubic γ-Al_2O_3 CIF data [13]. SEND patterns obtained with the 200 kV Tecnai F20 machine were acquired at a lateral (point-to-point) resolution of 1.5 nm using an external CCD camera focused on the small phosphorescent viewing screen. TEM-BF images, which were used specifically for facet analysis, were rotated according to an instrument specific diffraction imaging rotation. SEND patterns, obtained with the 200 kV JEM-F200 machine, were acquired at a lateral (point-to-point) resolution of 1 nm using an internal CCD camera. Orientation maps obtained from both instruments were corrected for noisy diffraction patterns and grain boundaries were added, assuming particles of at least 6 nm (i.e. 4 measurement points).

The VESTA 3 software package was used for three-dimensional visualization of crystal structures and particle morphologies [33].

3. Results and discussion

3.1. Characterization and thermostability of alumina samples

3.1.1. N_2-adsorption/desorption

Fig. 2a shows the N_2-adsorption/desorption isotherms for the fresh samples. All isotherms show type IV curves as a result of capillary condensation, taking place in the mesopores of the samples. The type H1 hysteresis loop obtained for all samples indicates fairly regular aggregate structures with uniform and cylindrical pores [34]. The resulting pore radius distributions are depicted in Fig. 2b. The obtained median pore radii are P100: 11.3 nm, TM100: 11.4 nm, and TH100: 14.6 nm. All samples exhibit the main population of mesopores above 10 nm, with significant fractions of pores with lower radius present in P100 and TM100. TH100 presents a narrower pore size distribution, along with the highest pore volume. Additional t-plot analyses of adsorption isotherms obtained at low relative pressures ($p/p_0 \geq 0.1$) revealed the absence of micropores in all samples [35].

The surface areas and pore volumes of the fresh and aged samples obtained from N_2 adsorption-desorption measurements are summarized in Table 1 and visualized in Fig. 3. The loss in surface area and pore volume with increasing temperature and ageing time follows a very similar trend for all materials up to 1100 °C and 10 h. The residual surface areas of all samples dropped markedly after ageing at 1000 °C for 3 h, with a further flat decrease upon ageing at 1100 °C for 3 and 10 h. It is worth mentioning that the duration of ageing at 1100 °C only had a small effect on the residual surface areas of all samples. A severe decrease in surface area was noted for P100 when the ageing temperature was raised to 1200 °C. TM100 was stable in the initial phase of ageing at 1200 °C, but distinct loss of surface area and pore volume was obtained after longer annealing time. The drop in pore volumes is less pronounced than the loss in surface areas up to 1100 °C, but it presents the same trend. The data obtained after ageing at 1200 °C for 10 h reveals the superior thermal stability of TH100. After this treatment, P100 had a residual surface area of 8 m^2/g and a very low pore volume of only 0.02 cm^3/g, whereas TH100 retained comparatively high surface area and pore volume ($S_{BET} = 60\ m^2/g$; $V_P = 0.52\ cm^3/g$). The thermostabilities in terms of residual surface areas and pore volumes after ageing follow the order TH100 > TM100 > P100.

3.1.2. Differential scanning calorimetry (DSC)

The formation of α-Al_2O_3 can be detected in differential scanning calorimetry experiments as it results from the first order θ → α phase transition and is therefore characterized by an exothermic peak, which appears above 1100 °C [36]. The DSC curves in the relevant temperature region are shown in Fig. 4. The exothermic peaks are centered at 1280 °C for P100, 1326 °C for TM100 and 1336 °C for TH100, pointing to a kinetic stabilization of TH100 compared to the other samples. The sharp peak of this sample reflects the higher level of homogeneity with respect to the aggregate structure in comparison to P100 and TM100.

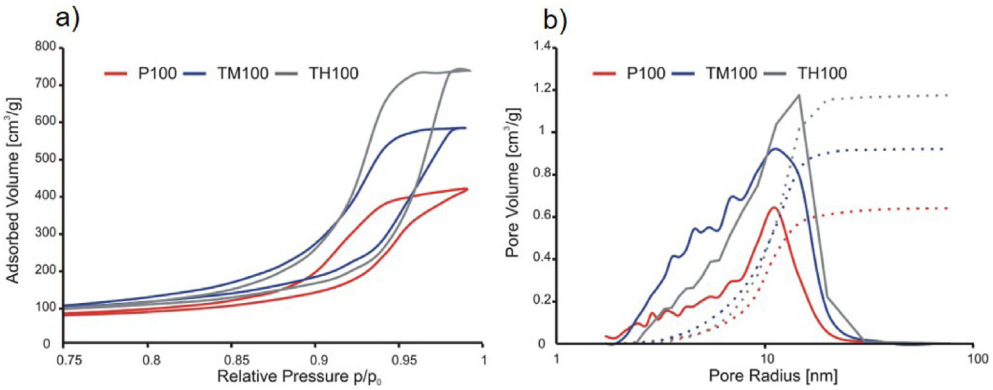

Fig. 2. a) Adsorption Isotherms b) Incremental (solid lines) and cumulative (dotted lines) pore radius distributions of fresh P100, TM100 and TH100.

Table 1
BET surface areas (S_{BET}) and pore volumes (V_p) of fresh and aged samples, obtained by N_2-adsorbtion/desorption measurements.

Fresh				1000 °C/3h			
	P100	TM100	TH100		P100	TM100	TH100
S_{BET} [m^2/g]	132	155	158	S_{BET} [m^2/g]	74	95	111
V_p [cm^3/g]	0.64	0.89	1.11	V_p [cm^3/g]	0.60	0.83	1.06
1100°C/3h				**1100°C/10h**			
	P100	**TM100**	**TH100**		**P100**	**TM100**	**TH100**
S_{BET} [m^2/g]	66	81	100	S_{BET} [m^2/g]	63	73	90
V_p [cm^3/g]	0.51	0.70	0.91	V_p [cm^3/g]	0.49	0.69	0.89
1200°C/3h				**1200°C/10h**			
	P100	**TM100**	**TH100**		**P100**	**TM100**	**TH100**
S_{BET} [m^2/g]	38	57	78	S_{BET} [m^2/g]	8	25	60
V_p [cm^3/g]	0.31	0.50	0.72	V_p [cm^3/g]	0.02	0.18	0.52

3.1.3. Powder X-Ray diffraction (XRD)

The powder X-ray patterns of the fresh and aged samples are shown in Fig. 5. and the phase compositions are summarized in Table 2.

The patterns of the fresh samples do not present significant differences. All fresh materials consist of γ-Al_2O_3 as the sole crystalline phase detectable by powder X-ray diffraction (Fig. 5a).

P100, TM100 and TH100 show specific differences with regards to occurrence and ratios of the alumina phases after ageing at elevated temperatures. θ-Al_2O_3 forms a main constituent in TH100 after ageing at 1000 °C for 3 h, as evidenced by the occurrence of the characteristic reflections located at approximately 17°, 19° and 48°, and the intensity ratios of the reflections in the range 31–34° (Fig. 5b). These features are much less pronounced in P100 and TM100 illustrating that θ-Al_2O_3 is only present in minor fractions. Weak reflections at approximately 18°, 22° and 42° are observed in the patterns of all samples (1000 °C/3h). Kovarik et al. reported a crystallographic refinement of the $\delta_{1/2}$-Al_2O_3 phases employing Density Functional Theory (DFT) methods, and their results strongly suggest that these reflections originate from the occurrence of δ-Al_2O_3, and predominantly the δ_1 phase [22]. The existence of residual γ-Al_2O_3 can neither reliably be confirmed nor ruled out via

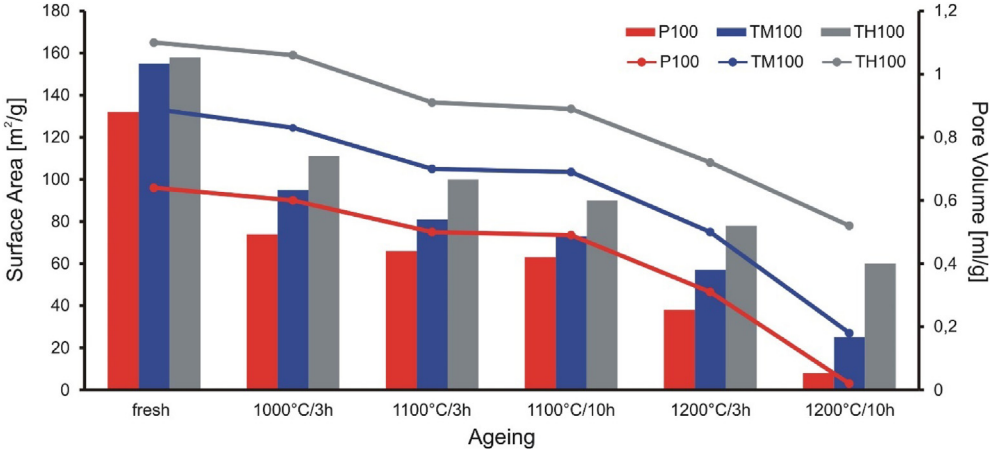

Fig. 3. Surface areas (columns) and pore volumes (lines) of fresh and aged samples.

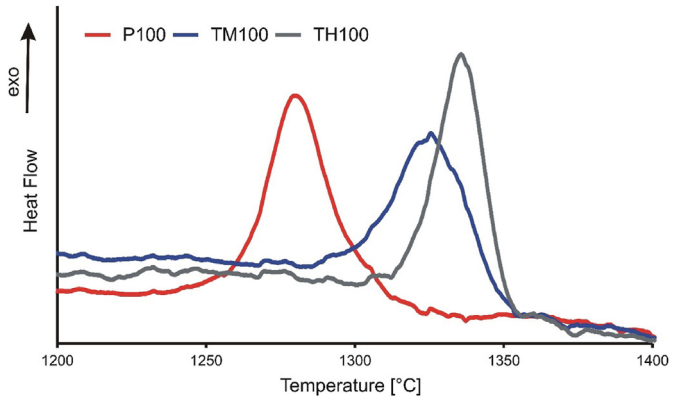

Fig. 4. DSC curves of fresh P100, TM100 and TH100.

powder X-ray diffraction. In the following, the presence of γ-Al_2O_3 is not considered once δ-Al_2O_3 is detected, and no further differentiation is made between the different δ-phases.

After calcination at 1100 °C for 3 h, all samples contain θ- and δ-Al_2O_3 but with considerably different ratios δ/θ. This is most obvious when comparing the intensities of the reflections in the range 44–48°. (Fig. 5c). The δ/θ ratio changed in all samples after ageing at 1100 °C for 10h, with a progressing evolution of the θ-phase (Fig. 5d). Additional weak reflections are obtained for P100 and TM100 in the range 26–30 °C, which are assigned to δ-Al_2O_3 in accordance with previous studies [22]. It is worth mentioning that phase-pure θ-Al_2O_3 is not obtainable in any of the samples, which confirms the finding that δ/θ-Al_2O_3 mixtures coexist in a broad temperature range [24].

The XRD patterns recorded after ageing at 1200 °C for 3 h reveal the superior thermostability of TM100, and especially TH100. Strong reflections of α-Al_2O_3 are detected in the corresponding powder pattern of

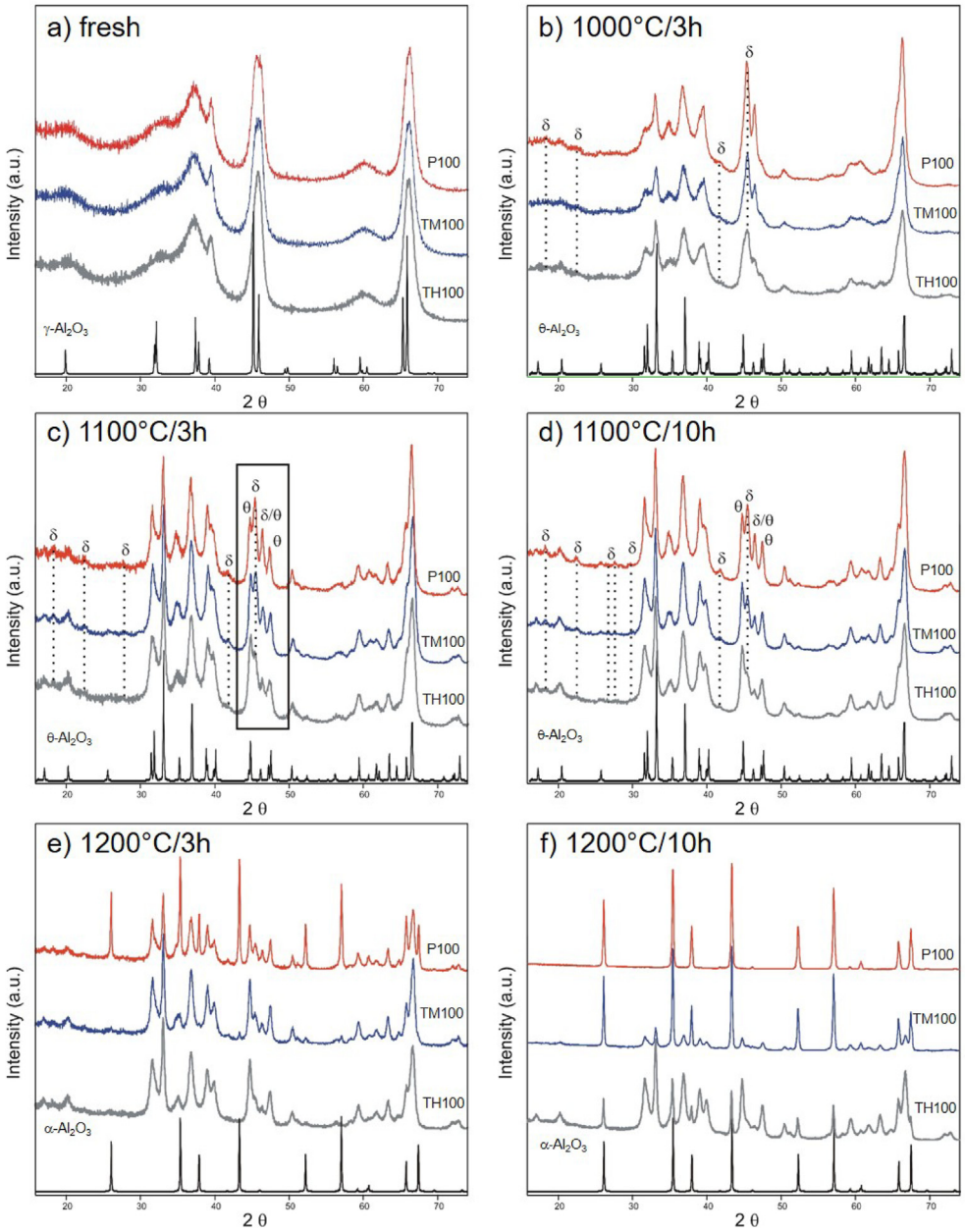

Fig. 5. X-ray powder patterns of fresh and aged samples. a) fresh samples, b) samples aged at 1000 °C for 3 h, c) samples aged at 1100 °C for 3 h, d) samples aged at 1100 °C for 10 h, e) samples aged at 1200 °C for 3 h, f) samples aged at 1200 °C for 10 h; calculated X-ray powder patterns of γ-Al_2O_3 (ICSD-99836) in a), θ-Al_2O_3 (ICSD-66560) in b) – d), and α-Al_2O_3 (ICSD-30024) in e) and f).

Table 2
Al_2O_3 phase compositions of the samples after calcination determined via powder X-ray diffraction. m: main phases; +: significant amounts; -: minor amounts; –: traces.

	fresh	1000 °C/ 3h	1100 °C/ 3h	1100 °C/ 10h	1200 °C/ 3h	1200°C/ 10h
P100	γ	δ^m/θ^-	δ^m/θ^+	δ^m/θ^+	$\theta^m/\alpha^m/\delta^-$	α
TM100	γ	δ^m/θ^-	θ^m/δ^+	δ^m/θ^m	$\theta^m/\delta^-/\alpha^-$	α^m/θ^+
TH100	γ	δ^m/θ^{-m}	θ^m/δ^-	θ^m/δ^-	θ^m/δ^-	θ^m/α^+

P100. These reflections are only weak in TM100 and absent in TH100 (Fig. 5e). After ageing at 1200 °C for 10 h, P100 quantitatively converted to α-Al_2O_3, which then also forms the main phase in TM100. In case of TH100 however, θ-Al_2O_3 is still the main component after this ageing procedure. The presence of α-Al_2O_3 as secondary phase is detected as well (Fig. 5f).

In summary, the order of α-Al_2O_3 formation rates was found to be P100 > TM100 > TH100, which is the reversal of the rates of θ-Al_2O_3 formation in the order TH100 > TM100 > P100. XRD and DSC data are in good agreement, as both analytical methods confirm the same trend in terms of α-alumina conversions. The onset of this event as detected via DSC appears at higher temperatures than detected by XRD, due to the much shorter exposure times at a given temperature in the DSC experiments. The results of N_2-adsorption/desorption experiments are consistent with these observations and illustrate that severe loss of surface areas coincides with the formation of α-Al_2O_3. This correlation is most obvious in case of P100 after ageing at 1200 °C for 10 h.

3.2. Morphologies and aggregate structures of γ-Al_2O_3 samples

3.2.1. Transmission electron microscopy bright field imaging (TEM-BF)

TEM bright field imaging was employed to study the morphologies and aggregate structures of the different fresh γ-Al_2O_3 samples (Fig. 6 and Fig. 7). If not further specified, the term "particle size" is used to address the long particle diameter across the principal basal plane of a platelet, whereas "thickness" refers to the dimension of a platelet parallel to the basal plane normal. It is worth mentioning that all particles consist of many very small crystallites, as a result of the pseudomorphic transition γ-AlOOH → γ-Al_2O_3 [37,38].

All samples contain particles with irregular 6-sided and almost rhombus-shaped 4-sided platelets. P100 predominately consists of large well-developed platelets. This sample exhibits the highest morphological diversity, so that also weakly facetted and much smaller particles are visible. Similar weakly facetted particles represent the main fraction in TH100, in which the least variety in terms of particle size and shape is visible. Particles with well-defined shape are observed much less frequently in TH100. TM100 is situated in between P100 und TH100, but the observed platelets with well-developed facets are distinctly smaller than in P100.

Representative individual particles are highlighted in Fig. 6, with models of idealized platelets incorporated in Fig. 6a and b. The top row displays examples of 6-sided platelets, and the bottom row highlights examples of 4-sided, nearly rhombus-shaped platelets for each P100, TM100 and TH100. Particles with similar shapes were also observed by other authors in γ-Al_2O_3 samples originating from precipitated and alkoxide-derived boehmites [30,37–40]. The thickness of the platelets was estimated by analyses of particles, with the main basal plane oriented parallel to the viewing direction, and ranges from 3 to 10 nm in all samples. The particle size was estimated to be 10–100 nm for P100, with a smaller fraction of even larger particles, 10–60 nm for TM100, and 10–40 nm for TH100.

The aggregate structures show substantial differences between P100, TM100 and TH100, stemming from the different particle size distributions and morphologies, which is illustrated in Fig. 7. The displayed sections were selected to illustrate the most important features of the three samples.

The large and well-developed platelets in P100 form stacks by oriented attachment via the main basal planes (red pointers in Fig. 7b and c). This type of arrangement leads to the generation of clusters with high densities and large contact areas between adjacent particles. In addition to the formation of these stacks, connection of particles via the less developed lateral facets is observed as well, thus forming sheet-like structures (blue pointers in Fig. 7b). The stacking of not perfectly overlapping particles, in combination with the lateral assembly, accounts for the creation of mesopores, as it can be seen in Fig. 7b (white pointer).

In contrast, the majority of TH100 particles is much smaller and

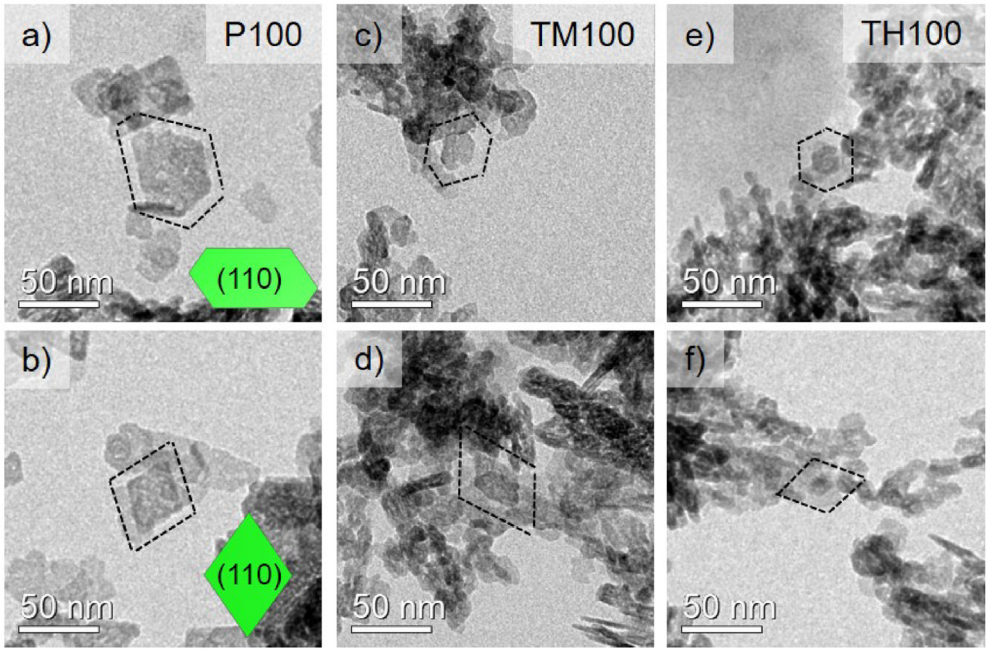

Fig. 6. TEM-BF images of a), b) P100, c), d) TM100, and e), f) TH00. Well-facetted particles are highlighted in black. Idealized 3D-models of 6- and 4-sided platelets are shown in a) and b).

shows a less pronounced plate-like shape. This morphology, in combination with the narrower particle size distribution, leads to a significantly less dense aggregate architecture, with a higher concentration of almost uniform mesopores (black pointers in Fig. 7h). This observation is also confirmed by the pore size distributions and pore volumes obtained by N_2-adsorption/desorption experiments. However, even this sample contains a minor population of particles with more pronounced plate-like morphology. These particles also seem to form sheets and arrangements with higher local densities (blue pointers in Fig. 7h, red pointers in Fig. 7i).

The TM100 sample displays features of both the P100, and the TH100 samples. Fig. 7e shows a region with a high concentration of platelets like those observed in P100, whereas a region with an aggregate structure comparable to TH100 is represented in Fig. 7f.

3.2.2. *Automated crystallite orientation mapping*

The inspection of TEM bright-field images provided a first impression of the particle size distribution of P100, TM100 and TH100. Automated crystallite orientation mapping (ACOM) by the means of scanning electron nanobeam diffraction (SEND) realized with ASTAR was employed for statistical analysis of particle size distributions.

In addition, the orientation maps generated by the ACOM provide additional insights on the formation of the different aggregate structures, and thus a more detailed and accurate description of the samples.

Fig. 8 displays the results of the particle size distribution analysis. As it can be seen, P100 shows the largest variety in particle sizes, followed by TM100, and TH100 exhibiting the narrowest particle size distribution. At the same time, TM100 and TH100 present a markedly higher fraction of small particles with diameters less than 15 nm. The presented data excludes datapoints with an orientation reliability of <15, as suggested by Rauch and Duft [41]. The observed values are in good agreement with the particle sizes and trends obtained by visual inspection of the TEM-BF images. Particle sizes obtained with ACOM using the full dataset confirmed the same trend with respect to the distribution width, but unreasonably large particle sizes were thus obtained: up to 170 nm for P100, up to 110 nm for TM100 and up to 100 nm for TH100. This shows that the misorientation of individual platelets in clusters with oriented attachment is often not significant enough to prompt ACOM to assign particle boundaries. These observations underline the usefulness of applying the orientation reliability. However, orientation analysis corrected accordingly might on the other hand lead to a wrong assignment of abundant large particles. The consideration of both statistics in combination with the visual inspection of TEM images thus appears to the most reasonable approach for particle size analyses.

Orientation maps of different sections of P100, TM100 and TH100 were collected to provide a better understanding of the particle morphologies and the formation of the aggregate structures.

Fig. 9 demonstrates that most of the particles in P100 are preferentially oriented close to <110> (green areas) or <121> (purple areas), stemming from the pronounced plate-type morphology. The color code of layered sheet-like structures confirms that the orientation of the particles in these arrangements is very similar. Additionally, formation of sheets by assembly of lateral facets can be observed as well. In these arrangements, the orientation of the particles is identical. A prominent example

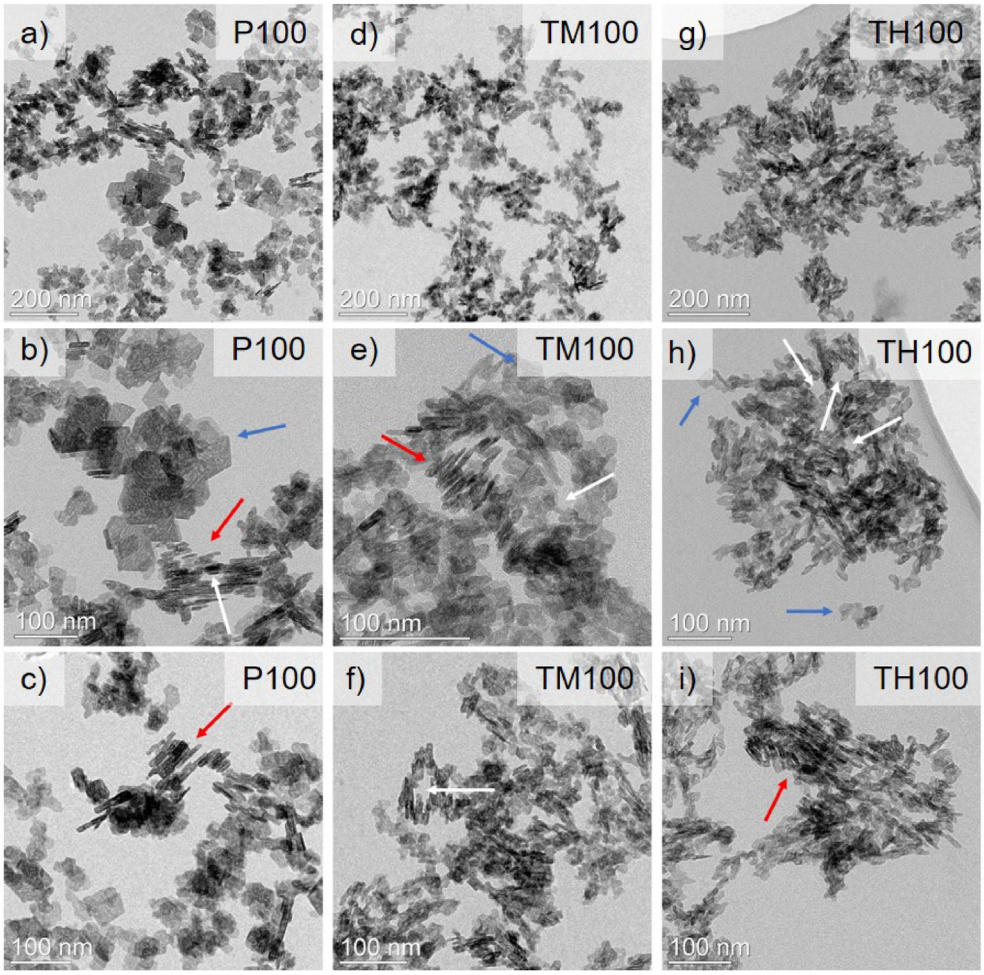

Fig. 7. TEM-BF images of a) – c) P100; d) – f) TM100, and g) – i) TH100. Red pointers: particle stacks, blue pointers: layered sheet-like structures, white pointers: mesopores.

for such a sheet, which is formed by attachment of lateral facets {111}, is highlighted ("X") in Fig. 9c. Details on facet indexing of this cluster are provided in Fig. S1.

ACOM reveals that the formation of dense regions results from oriented attachment of platelets in <110> direction via the main basal planes. This can be concluded from the dense cluster of aggregates in <100> orientation (red pointers in Fig. 9a).

In comparison to P100, orientation maps of TM100 (Fig. 10) show a noticeably lower but nevertheless significant fraction of particles in <110> orientation, which is indicative for a less pronounced plate-like shape and in accordance with the visual inspection of TEM-BF images. Comparable to P100, sheet-like arrangements in TM100 are predominantly formed by platelets with either <110> or <121> orientations. The formation of stacks in <110> direction by particles in or close to <111> (blue areas) and <100> (red areas) orientations can also be detected in TM100 but these dense clusters occur less frequent than in P100 and are also less developed (red pointer in Fig. 10a).

The orientation mappings of TH100 (Fig. 11) show distinct differences to TM100 and, even more clearly to P100. The particles in TH100 are more randomly oriented underpinning the much less developed plate-like morphology. Furthermore, the measurements suggest a significantly higher contribution of the lateral facets as indicated by the large fraction of particles in the corresponding <111> (blue) and <100> (red) orientations. Another important observation can be made when comparing clusters formed by lateral facets in P100 and TH100. In P100, particles with <100> and <111> orientations mostly form clusters with large interparticle contact areas and high densities whereas identically oriented particles in TH100 are found in more porous regions. Stacking in <110> direction via basal planes leading to dense structures is not observed in the orientation mappings of TH100, suggesting that the less developed plate-like shape hampers the formation of <110> layered clusters.

Interestingly, clusters built from the attachment of the main basal planes appear to be predominantly formed by similarly oriented particles color coded with either <111> or <100> directions in P100, TM100 and TH100. Combinations of particles in both orientations are only observed occasionally.

Extracts of P100 and TM100 orientation maps are highlighted in Fig. 12, to illustrate the formation of these aggregates with high densities in more detail. Moreover, 3D-models of 6-sided plate-like particles are displayed as well. Considering the presented TEM and ACOM measurements, irregular 6-sided plate-like morphology was assumed in these models, with {110} forming the main basal planes, and {100}, such as {111} forming the lateral facets. Accurate facet indexing is based on electron nanobeam diffraction patterns (Fig. S2 and S3). Particle facets are color-coded according to the inverse pole figure color key of the orientation maps, with green for <110>, blue for <111> and red for <100> oriented facets. The assignment of particle facets, as dictated by indexing the basal plane as (110), is summarized in Table 3.

The coordinate systems shown below the particle models illustrate the stacking direction (large green pointer) in the ACOM orientation maps and TEM-BF reference images respectively. They display the platelet specific lattice directions parallel to the principal ACOM orientation map coordinate system (X, Y, Z). Z (transmission direction) corresponds to the zone axis orientation of the observed local electron diffraction pattern, as indexed with ACOM, whereas X and Y correspond to equivalent lattice directions orthogonal to the observed zone axis.

The ACOM analyses of P100 and TM100 demonstrate the predominant presence of exposed {110} facets in most of the observed particles. The prevalent role of these basal planes has been reported about and rationalized before by several authors [37,42,43]. Moreover, the orientation analysis revealed <110> as the principal stacking directions, and therefore the crucial role of well-developed {110} facets in the generation of dense regions with large interparticle contact areas. Mesopores are mainly created by the assembly via the lateral {100} or {111} facets, in combination with oriented attachment of not perfectly overlapping

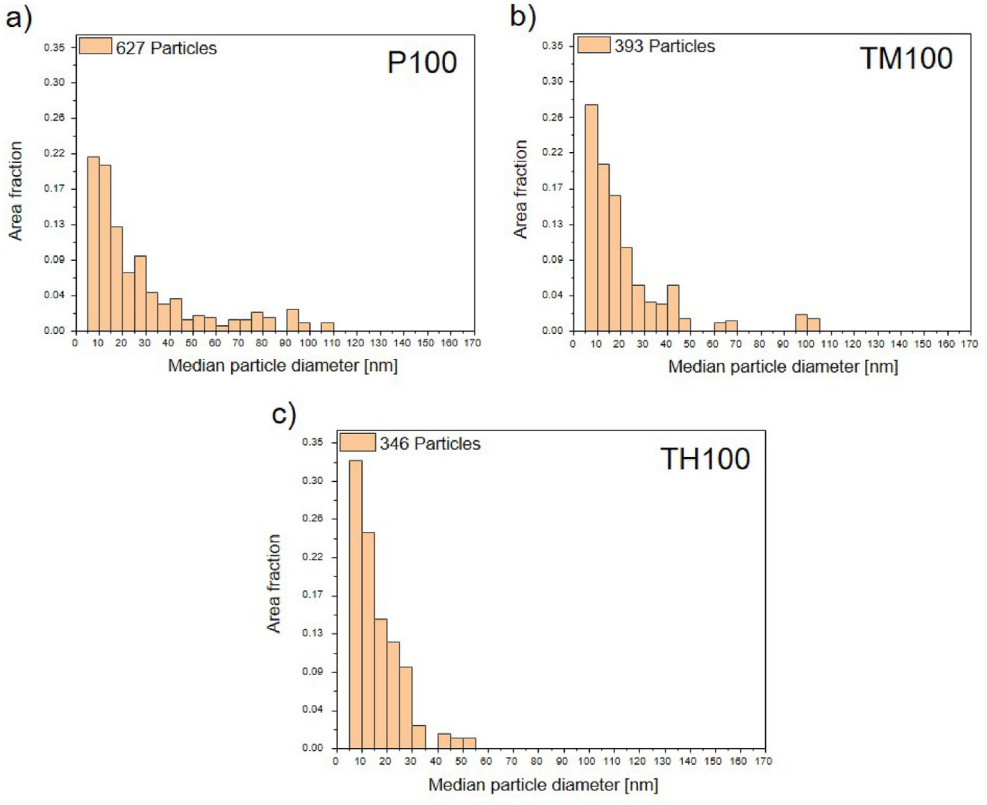

Fig. 8. ACOM particle size analysis a) P100, b) TM100, and c) TH100, excluding results with an orientation reliability of <15. Median particle diameter values are scaled in terms of area fraction.

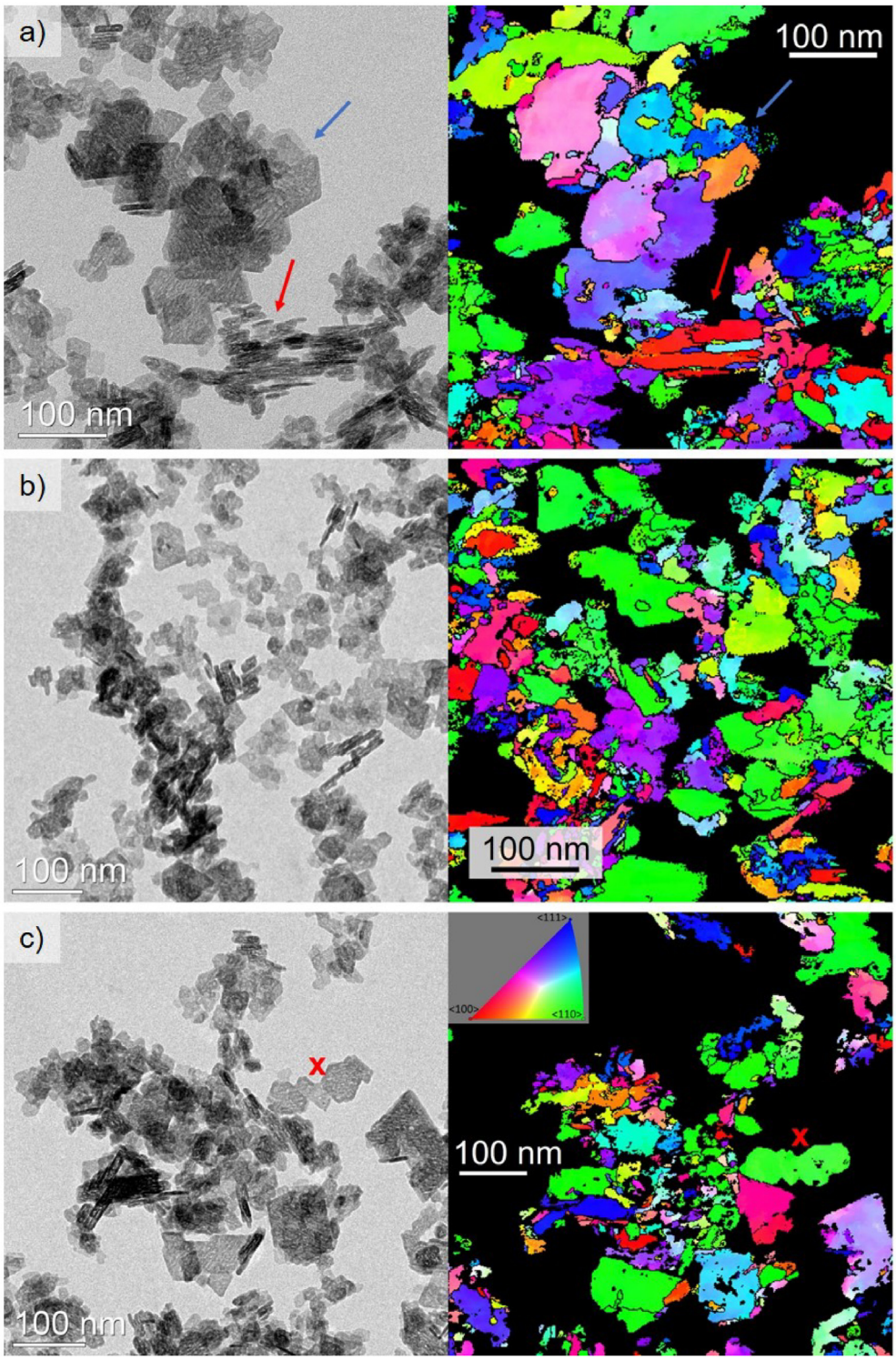

Fig. 9. TEM-BF images (left) and corresponding orientation maps (right) of P100 alumina particle groups. The orientation map color key in c) applies for all maps and refers to the inverse pole figure orientation along the optical axis. Red pointer: particle stacks, blue pointer: layered sheet-like structure, X: isolated sheet. Extracts of a) and c) are detailed in Fig. 12.

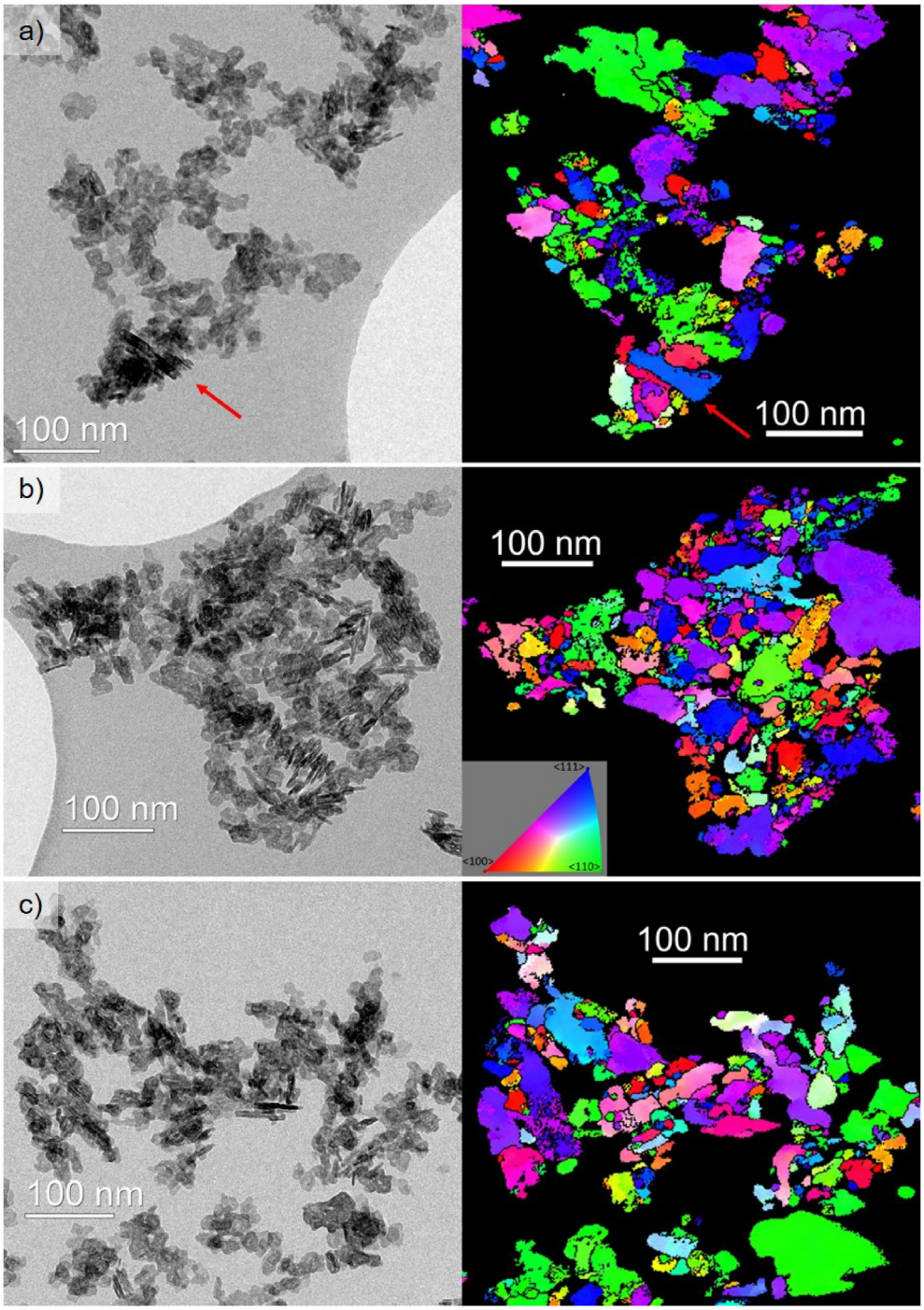

Fig. 10. TEM-BF images (left) and corresponding orientation maps (right) of TM100 alumina particle groups. The orientation map color key incorporated in b) applies for all maps and refers to the inverse pole figure orientation along the optical axis. Red pointer: particle stacks. Extracts of a) are detailed in Fig. 13.

platelets in <110> direction.

STEM-SE images of TH100 were collected to display the topographical features of TH100 (Fig. 13). From the images in combination with the orientation maps, two modes of particle arrangements can be distinguished.

1) Uniformly shaped particles with comparatively large {111} and {100} facets preferably form clusters via attachment of {110} facets (grey circle in Fig. 13b).
2) Particles with irregular shape seem to favor a more random orientation, including the attachment of lateral facets to {110} planes of adjacent particles ("house of cards structure" [36], white circle in Fig. 13b).

Both modes are obviously the result of the narrow particle size distribution, such as comparatively well-developed {100} and {111} facets, and lead to the generation of porous moieties.

The combined TEM-BF imaging and orientation analysis strongly suggests that the formation of dense [110] stacks tend to occur much less frequently than in P100 and TM100, due to the distinct particle form factor.

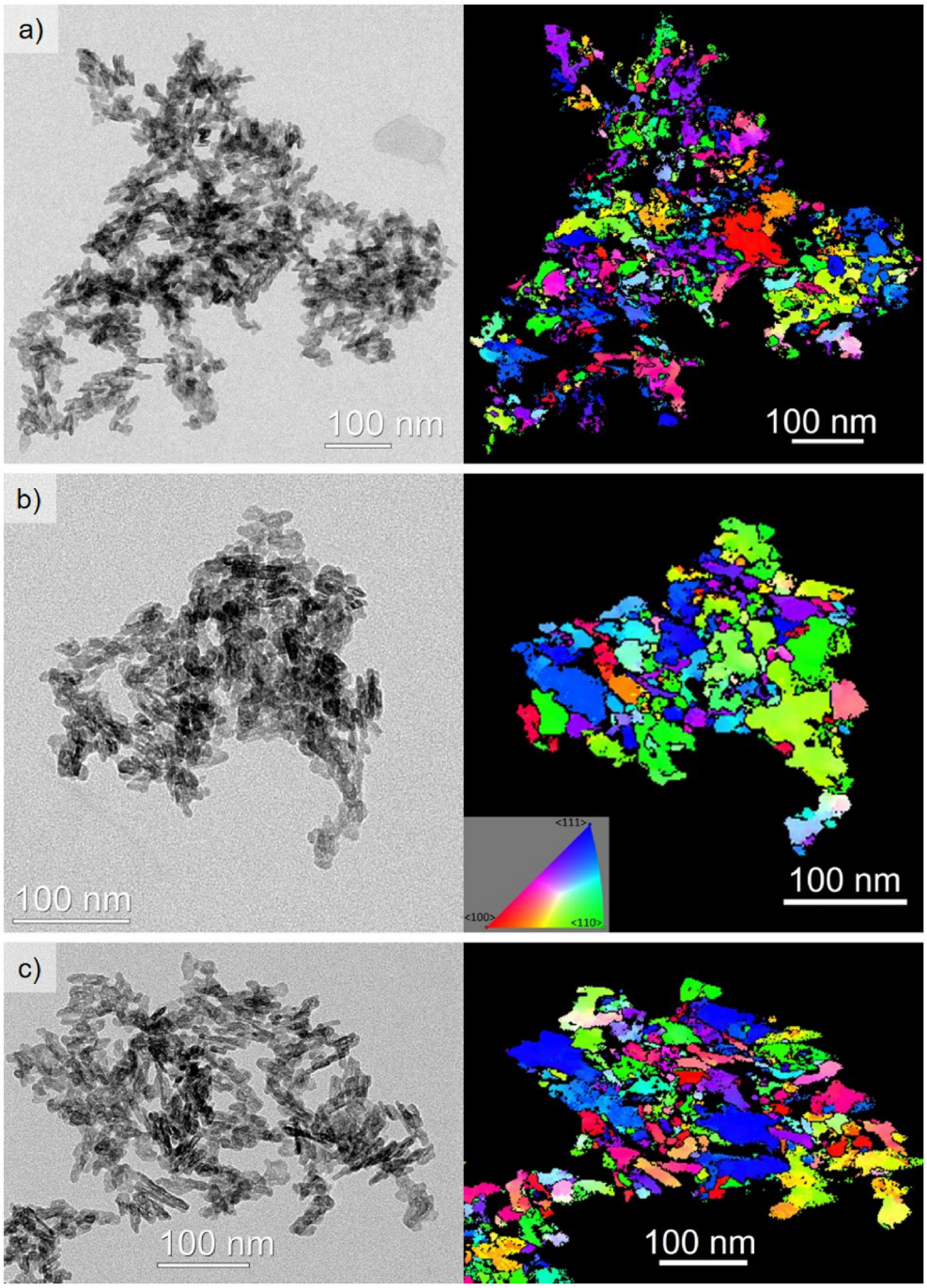

Fig. 11. TEM-BF images (left) and corresponding orientation maps (right) of TH100 alumina particle groups. The orientation map color key in b) applies for all maps and refers to the inverse pole figure orientation along the optical axis.

3.3. Correlation between morphology and thermostability

The presented data reveals that the morphology of primary particles and the resulting agglomerate structure has a crucial effect on the thermostability of mesoporous transition aluminas. The results of N_2-adsorbtion/desorption, DSC and XRD experiments confirm that the decrease in surface areas and the formation of α-Al_2O_3 follow the order P100 > TM100 > TH100. This trend correlates very well with the aggregate structures observed in TEM experiments, and can be rationalized by the well-understood mechanisms of sintering and the $\theta \rightarrow \alpha$ phase transition [26,27]. The surfaces of transition aluminas exhibit a high concentration of OH-groups partially substituting oxide ions. The progressive condensation of these surface hydroxyls upon calcination eventually leads to sintering and the formation of α-Al_2O_3 nuclei. In a first approximation, the number of hydroxyl-groups, and hence the expected rates of sintering, correlate with the BET surface areas of the initial transition aluminas. However, our data consistently demonstrates that the interparticle contact areas largely influence these thermally induced processes. Although the fresh BET surface areas of the γ-Al_2O_3 samples P100, TM100 and TH100 are very similar, the interparticle area in P100 is distinctly higher than in the other samples, due to the well-developed plate-like morphology of the particles, associated with the formation of dense stacks formed by the oriented attachment via the {110} main basal planes. The high contact area between adjacent

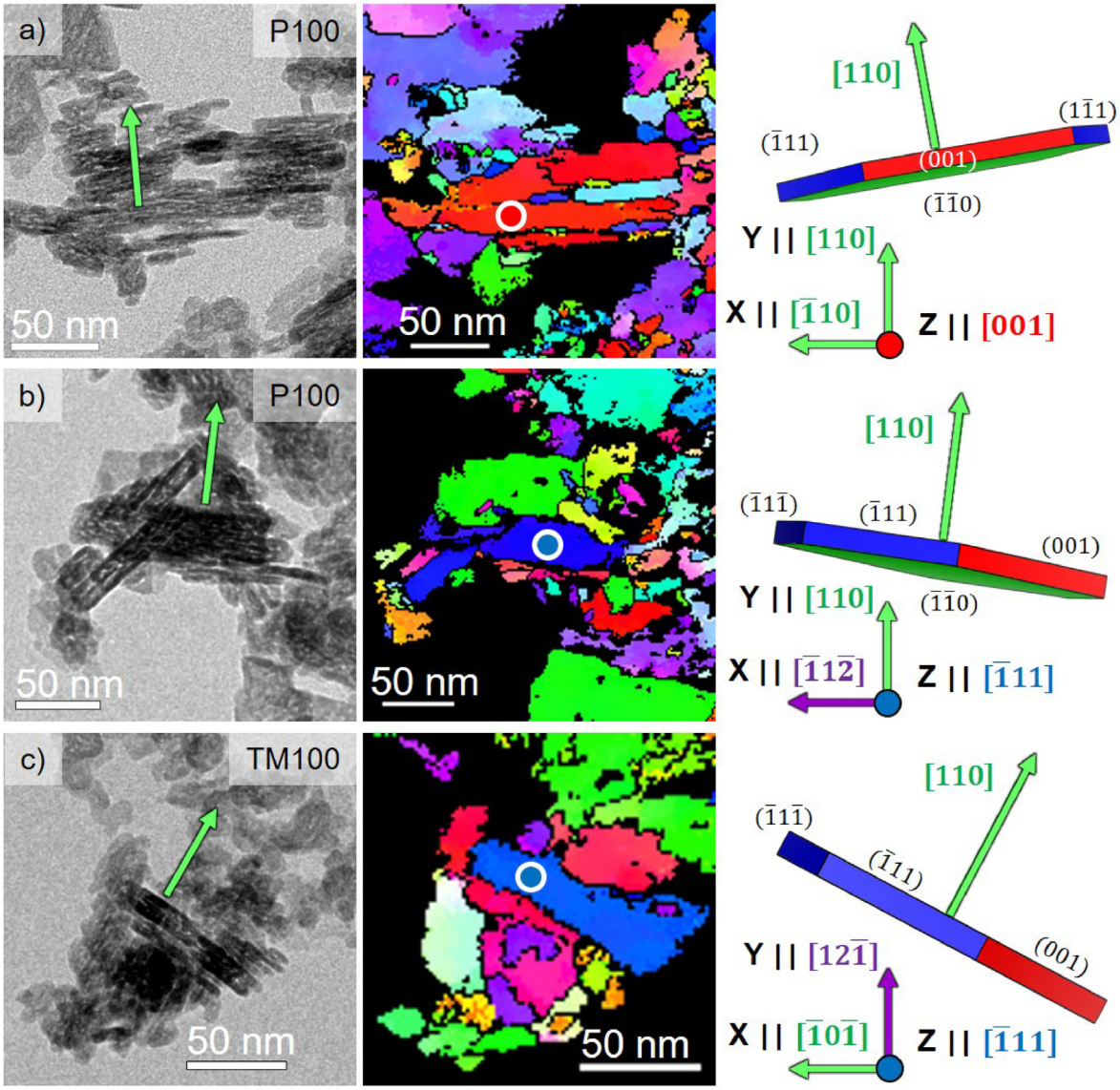

Fig. 12. TEM-BF and ACOM orientation map close-ups of stacked platelets. a) and b) P100, c) TM100. As illustrated by the 3D-models (110)/($\bar{1}\bar{1}$ 0) were selected to address the platelet basal facets with the [110] normal as the upward facing direction. The coordinate systems provide details on the 3D-orientation of the corresponding particles. The origin of the coordinate systems of the particles are indicated by a circle in the orientation maps.

particles favors the condensation of surface hydroxyls, resulting in sintering and the generation of α-Al_2O_3 nuclei at lower temperatures than in TM100 and particularly in TH100. The results demonstrate that a higher share of {100} and {111} facets in the total surface area, in combination with uniform morphologies and narrow particle size distributions, leads to more favorable aggregate structures characterized by high concentrations of mesopores and low interparticle contact areas. These findings are summarized in Fig. 14.

From XRD data it can be concluded that the δ → θ transformation in TH100 occurs at lower temperatures than in P100 and TM100. Kwak et al. uncovered that the formation of θ-Al_2O_3 is promoted by the existence of coordinatively unsaturated aluminium(II) species (pentacoordinated Al(III)) on the surface of {100} facets [44,45]. The presented ACOM data supports this finding. Although the relative contributions of {100} facets on the total surface area were not calculated, the lateral facets are clearly more developed in the order P100 < TM100 < TH100. This observation gains further relevance when considering the studies by Lee et al., who found that particularly pentacoordinated Al(III) species located on {100} facets contribute to improved catalyst performances, for instance in case of Pt–Al_2O_3 for benzene hydrogenation [40]. In the same work, the authors found that the special surface characteristics of δ/θ-Al_2O_3 lead to improved Pt dispersion and stability on this support. Our presented data illustrates the predominant existence of the δ/θ-phases over a wide temperature range in case of TH100, which is an important aspect in this regard, further underlining that the morphology control of transition aluminas is a valuable approach for the design of supported noble metal catalysts.

A common approach for improving the thermostability of transition aluminas is the addition of dopants, such as lanthanum oxide. The presence of large La^{3+} cations in the alumina lattice leads to significantly reduced volume diffusion in the solid, and thereby to higher activation energies for the formation of α-Al_2O_3. Moreover, La_2O_3 lowers the concentration of active sites for the formation of α-Al_2O_3 nuclei via reaction with pentacoordinate Al(III) species, yielding the perovskite-phase $LaAlO_3$. This phase is also formed by the reaction of La_2O_3 with Al(III) on T_d positions, whereby Al(III) is brought into octahedral coordination in the perovskite structure, resulting in a thermodynamic stabilization of 10 kj/mol [27,46–48].

Table 3
Indexing of particle facets. Specified colors refer to the inverse pole figure color key of the orientation maps in Figs. 9–11.

Basal planes (green)	Lateral facets (red)[a]	Lateral facets (blue)
(110)	(001)	$(\bar{1}11)$
$(\bar{1}\bar{1}0)$	$(00\bar{1})$	$(1\bar{1}\bar{1})$
		$(\bar{1}1\bar{1})$
		$(1\bar{1}1)$

[a] (001) and $(00\bar{1})$ belong to the {100} group of equivalent facets in the cubic crystal system.

Our studies suggest that fine-tuning of the particle morphology, together with the proper addition of dopants, is a suitable strategy to obtain transition aluminas which are suitable for catalyst applications demanding for very high thermal durability.

4. Conclusion

In previous studies, it has been found that transition aluminas with higher initial surface areas are less stable towards sintering and the formation of α-Al_2O_3 [27–29]. With this work, we supplement these findings by emphasizing the role of the aggregate structures, which originate from the assembly of primary particles with different morphologies. For this purpose, we compared alumina samples with very similar fresh surface areas and pore sizes, but with different pore volumes.

The results of our investigations consistently reveal that aggregate structures with high concentration of mesopores and low interparticle contact areas lead to transition aluminas with superior thermostability. Such aggregate architectures are built from particles characterized by a) less developed plate-like shape along with a high contribution of the lateral {100} and {111} facets, b) uniform morphology, and c) narrow size distribution.

It has been demonstrated that scanning electron nanobeam diffraction (SEND) realized with the ASTAR system is a powerful method for detailed

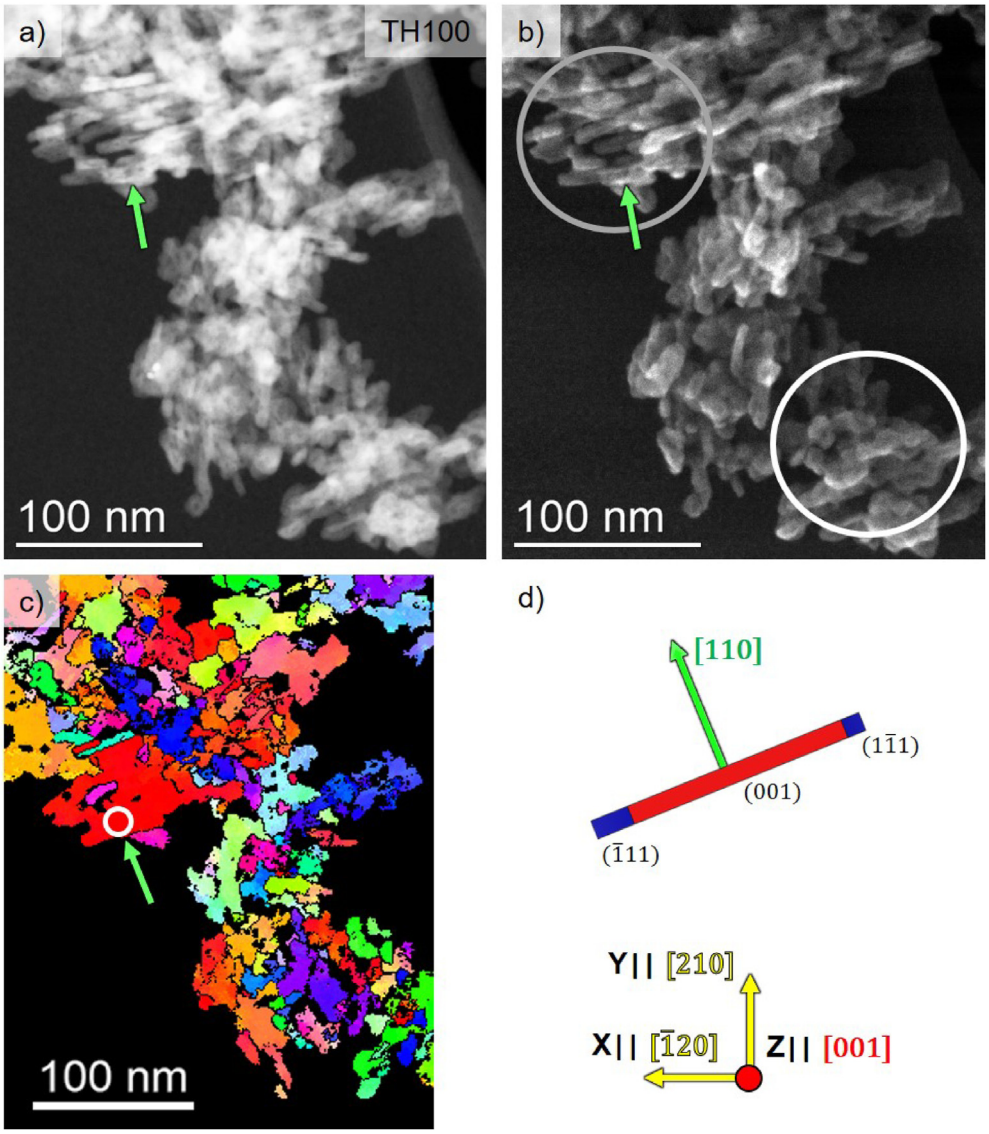

Fig. 13. Assembly of TH100 particles. a) STEM-ADF image, b) STEM-SE image, c) ACOM, and d) 3D-model. The coordinate system in d) provides details on the 3D-orientation of the corresponding particle. The origin of the coordinate system of the particle is indicated by a circle in the orientation map. Grey circle: assembly of uniform particles. White circle: assembly of irregular particles.

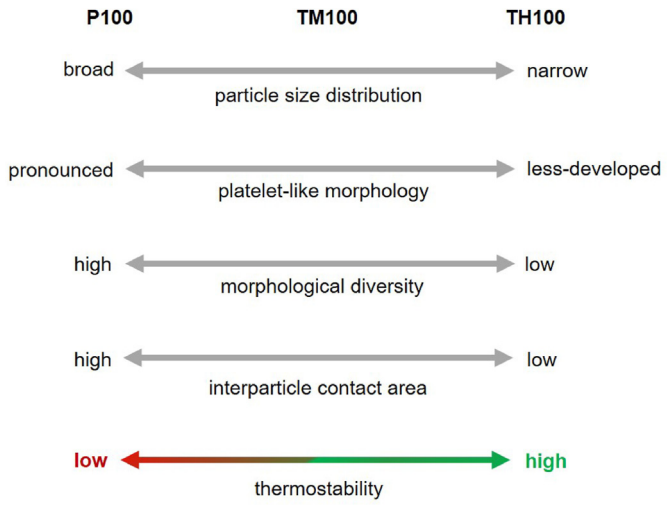

Fig. 14. Summary of the findings from morphological and thermostability studies.

analyses of the aggregate structure, and the suitability of this technique for crystallite phase mapping has just recently been demonstrated as well [49]. This suggests that hitherto not fully understood phenomena might effectively be investigated by this technique in more detail, e.g., the phase transformations γ-Al_2O_3 → δ-Al_2O_3 → θ-Al_2O_3 → α-Al_2O_3, and the morphological changes taking place during these processes.

CRediT authorship contribution statement

Marcos Schöneborn: Conceptualization, Investigation, Visualization, Supervision, Writing – original draft. **Jonas Werner:** Investigation, Visualization, Writing – review & editing. **Thomas Harmening:** Investigation, Writing – review & editing. **Thomas E. Weirich:** Resources, Writing – review & editing, Supervision.

Declaration of competing interest

The authors declare the following financial interests/personal relationships which may be considered as potential competing interests: The authors M. Schöneborn and T. Harmening are employees of SASOL Germany GmbH. The company produces the materials studied in this paper.

Acknowledgments

This work was supported by the German Federal Ministry of Education and Research (BMBF) under grant numbers 13XP5042A and 13XP5042B. The authors thank Dirk Worch and his team (SASOL Germany GmbH) for XRD and N_2-adsorption/desorption measurements, such as Kai Dölling for collecting the DSC data. Valuable suggestions provided by Karen Beckhusen and Dr. Malina Bilo are kindly acknowledged.

Appendix A. Supplementary data

Supplementary data to this article can be found online at https://doi.org/10.1016/j.jssc.2022.122906.

References

[1] E. Rytter, A. Holmen, On the support in cobalt Fischer–Tropsch synthesis—emphasis on alumina and aluminates, Catal. Today 275 (2016) 11–19, https://doi.org/10.1016/j.cattod.2015.11.042.
[2] M.R. Rahimpour, M. Jafari, D. Iranshahi, Progress in catalytic naphtha reforming process: a review, Appl. Energy 109 (2013) 79–93, https://doi.org/10.1016/j.apenergy.2013.03.080.
[3] R.J. Farrauto, Industrial catalysis: a practical guide, in: J.A. Kent (Ed.), Kent Riegel's Handb. Ind. Chem. Biotechnol., Springer US, Boston, MA, 2007, pp. 271–304, https://doi.org/10.1007/978-0-387-27843-8_7.
[4] M.V. Twigg, Catalytic control of emissions from cars, Catal. Today 163 (2011) 33–41, https://doi.org/10.1016/j.cattod.2010.12.044.
[5] R. Peters, J.L. Breuer, M. Decker, T. Grube, M. Robinius, R.C. Samsun, D. Stolten, Future power train solutions for long-haul trucks, Sustain. 13 (2021) 1–59, https://doi.org/10.3390/su13042225.
[6] J. Burre, D. Bongartz, L. Brée, K. Roh, A. Mitsos, Power-to-X: between electricity storage, e-production, and demand side management, Chem. Ing. Tech. 92 (2020) 74–84, https://doi.org/10.1002/cite.201900102.
[7] A. Arnberger, P. Grabner, M. Eder, B. Raser, Hydrogen combustion engine for CO_2-neutral commercial vehicles, ATZheavy Duty Worldw. 14 (2021) 36–41, https://doi.org/10.1007/s41321-021-0431-5.
[8] M. Richter, R. Fricke, R. Eckelt, Unusual activity enhancement of NO conversion over Ag/Al_2O_3 by using a mixed NH_3/H_2 reductant under lean conditions, Catal. Lett. 94 (2004) 115–118, https://doi.org/10.1023/B:CATL.0000019340.51510.ba.
[9] S. Fogel, P. Gabrielsson, H_2-assisted NH_3-SCR over Ag/Al_2O_3: an engine-bench study, Appl. Catal. B Environ. 158–159 (2014) 1–10, https://doi.org/10.1016/j.apcatb.2014.03.040.
[10] G. Xu, H. Wang, Y. Yu, H. He, Role of silver species in H_2-NH_3-SCR of NO_x over Ag/Al_2O_3 catalysts: operando spectroscopy and DFT calculations, J. Catal. 395 (2021) 1–9, https://doi.org/10.1016/j.jcat.2020.12.025.
[11] M.D. Argyle, C.H. Bartholomew, Heterogeneous catalyst deactivation and regeneration: a review, Catalysts 5 (2015), https://doi.org/10.3390/catal5010145, 145–269.
[12] L. Volpe, M. Boudart, Topotactic preparation of powders with high specific surface area, Catal. Rev. 27 (1985) 515–538, https://doi.org/10.1080/01614948508064232.
[13] R.-S. Zhou, R.L. Snyder, Structures and transformation mechanisms of the η, γ and θ transition aluminas, Acta Crystallogr. Sect. B Struct. Sci. 47 (1991) 617–630, https://doi.org/10.1107/S0108768191002719.
[14] B.C. Lippens, J.H. de Boer, Study of phase transformations during calcination of aluminum hydroxides by selected area electron diffraction, Acta Crystallogr. 17 (1964) 1312–1321, https://doi.org/10.1107/s0365110x64003267.
[15] I. Levin, D. Brandon, Metastable alumina polymorphs: crystal structures and transition sequences, J. Am. Ceram. Soc. 81 (2005) 1995–2012, https://doi.org/10.1111/j.1151-2916.1998.tb02581.x.
[16] I. Levin, L.A. Bendersky, D.G. Brandon, M. Rühle, Cubic to monoclinic phase transformations in alumina, Acta Mater. 45 (1997) 3659–3669, https://doi.org/10.1016/S1359-6454(97)00040-2.
[17] K.P. Sinha, A.P.B. Sinha, Vacancy distribution and bonding in some oxides of spinel structure, J. Phys. Chem. 61 (1957) 758–761, https://doi.org/10.1021/j150552a013.
[18] G. Paglia, C.E. Buckley, A.L. Rohl, B.A. Hunter, R.D. Hart, J.V. Hanna, L.T. Byrne, Tetragonal structure model for boehmite-derived γ-alumina, Phys. Rev. B 68 (2003), 144110, https://doi.org/10.1103/PhysRevB.68.144110.
[19] L. Samain, A. Jaworski, M. Edén, D.M. Ladd, D.-K.K. Seo, F. Javier Garcia-Garcia, U. Häussermann, Structural analysis of highly porous γ-Al_2O_3, J. Solid State Chem. 217 (2014) 1–8, https://doi.org/10.1016/j.jssc.2014.05.004.
[20] V. Jayaram, C.G. Levi, The structure of δ-alumina evolved from the melt and the γ → δ transformation, Acta Metall. 37 (1989) 569–578, https://doi.org/10.1016/0001-6160(89)90240-X.
[21] Y. Repelin, E. Husson, Etudes structurales d'alumines de transition. I-alumines gamma et delta, Mater. Res. Bull. 25 (1990) 611–621, https://doi.org/10.1016/0025-5408(90)90027-Y.
[22] L. Kovarik, M. Bowden, A. Genc, J. Szanyi, C.H.F. Peden, J.H. Kwak, Structure of δ-alumina: toward the atomic level understanding of transition alumina phases, J. Phys. Chem. C 118 (2014) 18051–18058, https://doi.org/10.1021/jp500051j.
[23] L. Kovarik, M. Bowden, D. Shi, N.M. Washton, A. Andersen, J.Z. Hu, J. Lee, J. Szanyi, J.H. Kwak, C.H.F. Peden, Unraveling the origin of structural disorder in high temperature transition Al_2O_3: structure of θ-Al_2O_3, Chem. Mater. 27 (2015) 7042–7049, https://doi.org/10.1021/acs.chemmater.5b02523.
[24] L. Kovarik, M. Bowden, A. Andersen, N.R. Jaegers, N. Washton, J. Szanyi, Quantification of high-temperature transition Al_2O_3 and their phase transformations, Angew. Chem. 132 (2020) 21903–21911, https://doi.org/10.1002/ange.202009520.
[25] S. Geller, Crystal structure of β-Ga_2O_3, J. Chem. Phys. 33 (1960) 676–684, https://doi.org/10.1063/1.1731237.
[26] D.S. Tucker, Gamma-to- alpha transformation in spherical aluminum oxide powders, J. Am. Ceram. Soc. 68 (1985) 163–164.
[27] P. Burtin, M. Pijolat, M. Soustelle, D. Recherches, Influence of surface area and additives on the thermal stability of transition alumina catalyst supports. II: kinetic model and interpretation, Appl. Catal. 34 (1987) 239–254.
[28] H. Arai, M. Machida, Thermal stabilization of catalyst supports and their application to high-temperature catalytic combustion, Appl. Catal. A Gen. 138 (1996) 161–176, https://doi.org/10.1016/0926-860X(95)00294-4.
[29] T. Tsukada, H. Segawa, A. Yasumori, K. Okada, Crystallinity of boehmite and its effect on the phase transition temperature of alumina, J. Mater. Chem. 9 (1999) 549–553, https://doi.org/10.1039/a806728g.
[30] J. Lee, H. Jeon, D.G. Oh, J. Szanyi, J.H. Kwak, Morphology-dependent phase transformation of γ-Al_2O_3, Appl. Catal. A Gen. 500 (2015) 58–68, https://doi.org/10.1016/J.APCATA.2015.03.040.

[31] D.R.G. Mitchell, B. Schaffer, Scripting-customised microscopy tools for digital Micrograph™, Ultramicroscopy 103 (2005) 319–332, https://doi.org/10.1016/j.ultramic.2005.02.003.
[32] E.F. Rauch, M. Véron, J. Portillo, D. Bultreys, Y. Maniette, S. Nicolopoulos, Automatic crystal orientation and phase mapping in TEM by precession diffraction, Microsc. Anal. 22 (2008) S5–S8.
[33] K. Momma, F. Izumi, VESTA 3 for three-dimensional visualization of crystal, volumetric and morphology data, J. Appl. Crystallogr. 44 (2011) 1272–1276, https://doi.org/10.1107/S0021889811038970.
[34] M. Thommes, K. Kaneko, A.V. Neimark, J.P. Olivier, F. Rodriguez-Reinoso, J. Rouquerol, K.S.W. Sing, Physisorption of gases, with special reference to the evaluation of surface area and pore size distribution (IUPAC Technical Report), Pure Appl. Chem. 87 (2015) 1051–1069, https://doi.org/10.1515/pac-2014-1117.
[35] P. Voogd, J.J.F. Scholten, H. van Bekkum, Use of the t-plot—de Boer method in pore volume determinations of ZSM-5 type zeolites, Colloid. Surface. 55 (1991) 163–171, https://doi.org/10.1016/0166-6622(91)80090-B.
[36] H. Schaper, L.L. Van Reijen, A quantitative investigation of the phase transformation of gamma to alpha alumina with high temperature DTA, Thermochim. Acta 77 (1984) 383–393, https://doi.org/10.1016/0040-6031(84)87077-X.
[37] J. Lee, E.J. Jang, H.Y. Jeong, J.H. Kwak, Critical role of (100) facets on γ-Al_2O_3 for ethanol dehydration: combined efforts of morphology-controlled synthesis and TEM study, Appl. Catal. A Gen. 556 (2018) 121–128, https://doi.org/10.1016/j.apcata.2018.02.018.
[38] L. Kovarik, A. Genc, C. Wang, A. Qiu, C.H.F. Peden, J. Szanyi, J.H. Kwak, Tomography and high-resolution electron microscopy study of surfaces and porosity in a plate-like γ-Al_2O_3, J. Phys. Chem. C 117 (2013) 179–186, https://doi.org/10.1021/jp306800h.
[39] J. Lee, E.J. Jang, J.H. Kwak, Acid-base properties of Al_2O_3: effects of morphology, crystalline phase, and additives, J. Catal. 345 (2017) 135–148, https://doi.org/10.1016/j.jcat.2016.11.025.
[40] J. Lee, E.J. Jang, J.H. Kwak, Effect of number and properties of specific sites on alumina surfaces for Pt-Al_2O_3 catalysts, Appl. Catal. A Gen. 569 (2019) 8–19, https://doi.org/10.1016/j.apcata.2018.10.004.
[41] E.F. Rauch, A. Duft, Orientation maps derived from TEM diffraction patterns collected with an external CCD camera, Mater. Sci. Forum 495–497 (2005) 197–202. https://doi.org/10.4028/www.scientific.net/MSF.495-497.197.
[42] A. Reller, D.L. Cocke, High resolution transmission electron microscopic (HRTEM) determination of the preferentially exposed faces on gamma-Al_2O_3 and eta-Al_2O_3, Catal. Lett. 2 (1989) 91–95.
[43] M. Digne, P. Sautet, P. Raybaud, P. Euzen, H. Toulhoat, Use of DFT to achieve a rational understanding of acid-basic properties of γ-alumina surfaces, J. Catal. 226 (2004) 54–68, https://doi.org/10.1016/j.jcat.2004.04.020.
[44] J.H. Kwak, J. Hu, A. Lukaski, D.H. Kim, J. Szanyi, C.H.F. Peden, Role of pentacoordinated Al^{3+} ions in the high temperature phase transformation of γ-Al_2O_3, J. Phys. Chem. C 112 (2008) 9486–9492, https://doi.org/10.1021/jp802631u.
[45] J.H. Kwak, C.H.F. Peden, J. Szanyi, Using a surface-sensitive chemical probe and a bulk structure technique to monitor the γ- to θ-Al_2O_3 phase transformation, J. Phys. Chem. C 115 (2011) 12575–12579, https://doi.org/10.1021/jp203541a.
[46] M. Ozawa, M. Kimura, A. Isogai, Thermal stability and characterization of γ-Al_2O_3 modified with rare earths, J. Less Common. Met. 162 (1990) 297–308, https://doi.org/10.1016/0022-5088(90)90345-K.
[47] B. Béguin, E. Garbowski, M. Primet, Stabilization of alumina by addition of lanthanum, Appl. Catal. 75 (1991) 119–132, https://doi.org/10.1016/S0166-9834(00)83128-0.
[48] J.S. Church, N.W. Cant, D.L. Trimm, Stabilization of aluminas by rare earth and alkaline earth ions, Appl. Catal. A Gen. 101 (1993), 105–1196.
[49] S.I. Ecker, J. Dornseiffer, J. Werner, H. Schlenz, Y.J. Sohn, F.S. Sauerwein, S. Baumann, H.J.M. Bouwmeester, O. Guillon, T.E. Weirich, W.A. Meulenberg, Novel low-temperature lean NO_x storage materials based on $La_{0.5}Sr_{0.5}Fe_{1-x}M_xO_{3-\delta}/Al_2O_3$ infiltration composites (M = Ti, Zr, Nb), Appl. Catal. B Environ. 286 (2021), 119919, https://doi.org/10.1016/j.apcatb.2021.119919.